Journal of Applied Physics

# Phonon limited anisotropic quantum transport in phosphorene field effect transistors

Cite as: J. Appl. Phys. **126**, 114502 (2019); https://doi.org/10.1063/1.5109057
Submitted: 06 May 2019 . Accepted: 27 August 2019 . Published Online: 17 September 2019

Madhuchhanda Brahma, Arnab Kabiraj, Marc Bescond, and Santanu Mahapatra

Journal of Applied Physics ARTICLE scitation.org/journal/jap

# Phonon limited anisotropic quantum transport in phosphorene field effect transistors

Cite as: J. Appl. Phys. **126**, 114502 (2019); doi: 10.1063/1.5109057
Submitted: 6 May 2019 · Accepted: 27 August 2019 ·
Published Online: 17 September 2019

View Online Export Citation CrossMark

Madhuchhanda Brahma,[1,2] Arnab Kabiraj,[2] Marc Bescond,[3] and Santanu Mahapatra[2,a)]

## AFFILIATIONS

[1]Centre for Nanoscience and Engineering, Indian Institute of Science, Bangalore 560012, India
[2]Nanoscale Device Research Laboratory, Department of Electronic Systems Engineering, Indian Institute of Science, Bangalore 560012, India
[3]LIMMS, CNRS-UMI 2820, Institute of Industrial Science, University of Tokyo, 153-8505 Tokyo, Japan

[a)]**Electronic mail:** santanu@iisc.ac.in

## ABSTRACT

Electron-phonon coupling limited transport in phosphorene metal oxide semiconductor field effect transistors (MOSFETs) is studied along the armchair (AC) and zigzag (ZZ) directions. In a multiscale approach, the unit cell of phosphorene is first relaxed, and the band structure is calculated using hybrid density functional theory (DFT). The transport equations are then solved quantum mechanically under the non-equilibrium Green's function formalism using DFT-calibrated two-band $\mathbf{k}\cdot\mathbf{p}$ hamiltonian. The treatment of electron-phonon scattering is done under the self-consistent Born approximation in conjunction with deformation potential theory. It is found that optical phonon modes are largely responsible for degradation of ON-current apart from p-channel AC MOSFET where acoustic phonon modes play a stronger role. It is further observed that electron-phonon scattering is more pronounced in the ZZ direction, whereas the diffusive ON-current of p-MOSFET in a given direction is higher than n-MOSFET. Further study on the complex band structure of phosphorene reveals band wrapping within the bandgap region in the AC direction and multiple crossings in the ZZ direction. This signifies strong phonon-assisted tunneling in the ZZ direction in comparison with the AC direction. For completeness, drain current in the AC tunnel field effect transistor is calculated, and electron-phonon scattering is observed only in the near vicinity of the OFF-current.



## I. INTRODUCTION

Atomically thin two-dimensional (2D) layered materials have ushered in a new era in the field of semiconductor device and technology. These materials and their potential applications for transistor technologies are being studied both experimentally and theoretically. Most of these 2D materials such as hBN, phosphorene, and transition metal dichalcogenides (TMDs), like $MoS_2$, $WS_2$, $MoSe_2$, $WSe_2$, and $MoTe_2$,[1–6] are being extensively explored as an alternative channel material for MOSFET, in order to meet the Moore's law projections.

Among these materials, phosphorene, a single atomic layer of black phosphorus with a puckered honeycomb lattice structure,[4,5] has warranted special interest for its highly anisotropic transport properties. It has also resulted in successful fabrication of transistors.[4,5,7–11] Theoretical assessments[12–16] reveal that phosphorene MOSFETs outperform the TMD based MOSFETs in terms of ON-current requirements and subthreshold swing characteristics. The noteworthy performance of phosphorene MOSFETs is attributed to its very low effective mass along the armchair direction.

Most of the theoretical studies on phosphorene FETs have been limited to ballistic transport. A few recent articles have reported the performance of phosphorene MOSFET under electron-phonon scattering.[15,16] In this work, we present further insights into the phonon-limited transport of phosphorene MOSFETs. In addition, we inspect the effect of electron-phonon scattering on the performance of the tunnel field effect transistor (TFET), which has attracted attention for low-power applications. The key findings of our study are as follows:

- We investigate the individual effect of different phonon modes on the drain current of the devices. Results suggest that in n-MOSFETs along the armchair direction, acoustic phonon mode plays a dominant role in the reduction of ON-current, which is uncommon for other materials.

- In the ballistic regime, along a specific channel orientation, ON-state current in n-MOSFETs is either comparable (in armchair) to or greater (in zigzag) than p-MOSFETs. This behavior reverses in the dissipative regime.
- The complex band structure demonstrates distinctly different characteristics along the two directions from the same symmetry point of the material, namely, dominant imaginary band wrapping between conduction and valence band edges along armchair directions and multiple complex band crossings along the zigzag direction.

Here, nonequilibrium Green's function (NEGF) equations expressed in the self-consistent Born approximation (SCBA) are used to calculate transport in n- and p-type phosphorene MOSFETs along both armchair (AC) and zigzag (ZZ) directions as well as in p-i-n tunnel FET. The paper is organized as follows. In Sec. II, the simulation methodology is described followed by Sec. III where the effect of different electron-phonon interactions on the device transfer characteristics is pointed out. We finally draw our concluding remarks in Sec. IV. The present work is an extended version of our recent presentation,[17] which was based on single band effective mass hamiltonian and limited to n-channel MOSFETs.

## II. METHODOLOGY

A schematic representation of the device cross section under consideration is shown in Fig. 1. The effective oxide thickness (EOT) is chosen as 0.41 nm and supply bias $V_D = 0.64$ V, according to the ITRS 2013 specifications.[18] The length $L_{CH}$ of the undoped channel is taken equal to the gate length $L_G$, which is 20 nm. In the case of MOSFET, 20 nm long source and drain extensions are uniformly doped at $3 \times 10^{13}/cm^2$, whereas in TFET, they are doped at $2 \times 10^{13}/cm^2$ (p type) and $1 \times 10^{13}/cm^2$ (n type), respectively. Thickness of the phosphorene slab as extracted from the atomic configuration used in density functional theory (DFT) calculations turns to be 0.6 nm. The OFF-state current ($I_{OFF}$) at zero gate voltage ($V_G$) is set at 100 nA/$\mu$m in MOSFET and at 10 nA/$\mu$m in TFET by choosing an appropriate gate work function.

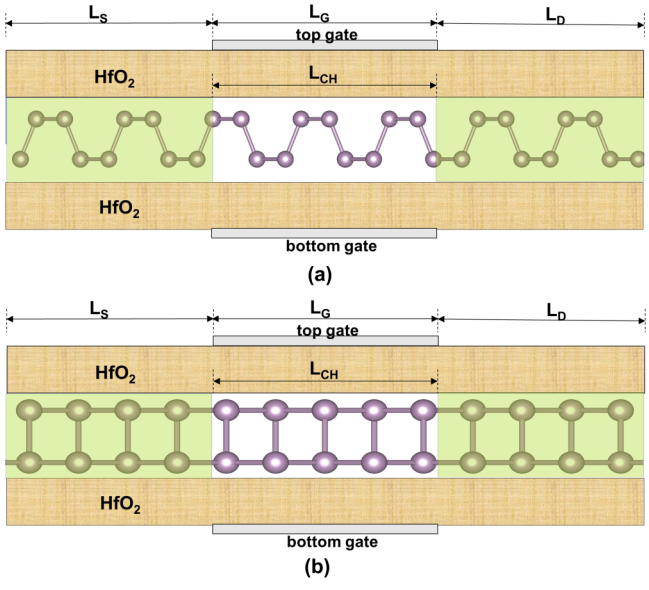


**FIG. 1.** Cross section of double-gate phosphorene FET with the transport direction as (a) armchair and (b) zigzag. $L_{CH}$ denotes the channel length, which is set equal to the gate length $L_G$. The channel is undoped, while the source and drain extensions (shaded) are uniformly doped in MOSFET and p and n types, respectively, in TFET. The dielectric constant of gate oxide $HfO_2$ is 25 and of phosphorene is 1.12.[19]

DFT calculations are performed to evaluate the electronic band structure, carrier effective mass, and bandgap values. The calculations are carried out using generalized gradient approximation (GGA) as implemented in the code VASP[20,21] with the PAW[22] method using the Perdew-Burke-Ernzerhof (PBE)[23] exchange correlation and the Heyd-Scuseria-Ernzerhof (HSE)[24] hybrid functional. The wavefunctions obtained from the PBE calculations are only used as a starting point in the HSE calculations. All the structural as well as electronic properties except the complex band structure (CBS) and phonon spectrum are determined from the HSE calculations. $3s^2\ 3p^3$ electrons of phosphorus are treated as valence electrons and expanded in plane wave basis set. A cutoff energy of 400 eV is used, a Γ-centered 15× 13× 1 (in X, Y, and Z directions) k-mesh is found to be suitable to sample the Brillouin zone for structural relaxations, and a denser k-mesh of 33× 29 ×1 is used for static calculations. Electronic convergence is achieved when the difference in energy of successive electronic steps becomes less than $10^{-6}$ eV, whereas the structural geometry is optimized until the maximum force on every atom falls below 0.01 eV/Å. A large vacuum space of more than 20 Å in the direction of Z is applied to avoid any interaction between successive layers. Phonon calculations are done using the code Phonopy,[25] which uses the atomic forces calculated from VASP based on density functional perturbation theory (DFPT) applied to a $2 \times 2$ phosphorene unit cell using a $27 \times 25 \times 1$ k-mesh. For generating CBS, DFT calculations are performed using Atomistix Tool Kit (ATK).[26] The accuracy of the calculations largely depends on the selection of norm-conserving pseudopotentials and numerical linear combination of atomic orbital (LCAO) basis sets in this case. GGA is employed as the exchange correlation in conjunction with the PBE functional. The "SG15" norm-conserving pseudopotentials with "medium" basis sets have been used. The optimized "SG15" provide smooth pseudopotentials with multiple projectors and nonlinear core corrections.[27,28] A k-mesh with a density of 6 Å along every lattice vectors is chosen, and a cutoff energy of 60 Hartree is employed. In order to obtain the CBS along AC and ZZ directions, the phosphorene surface is cleaved along [100] and [010].

Lattice parameters obtained after structure optimization and further used for bandstructure calculations are a = 4.57(4.62) Å and b = 3.27(3.29) Å for HSE(PBE) functional based DFT. The value of the bandgap obtained by using PBE functional is 0.9 eV and from HSE is 1.61 eV. All these values are in good agreement with previous reports.[29,30] The classical local or semilocal DFT is known to severely underestimate the bandgap of a material and can derive inaccurate structural parameters as well. The HSE hybrid functional includes 25% of the Fock nonlocal exact exchange energy for short-range interactions, which overcomes these limitations of local and semilocal DFT, and provides a good estimation of electronic as well as structural parameters for most systems. However, calculation of the Fock exchange increases the computational cost

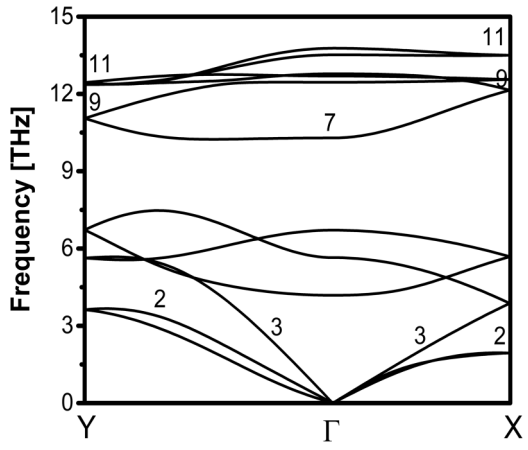


**FIG. 2.** Phonon dispersion of phosphorene calculated by density functional theory. The different phonon branches are numbered according to Ref. 31, wherein 2 and 3 are acoustic phonon modes, while the remaining are optical modes.

manifold and is thus not suitable for complex band structure calculations. On the other hand, HSE functional based DFT data are used for transport calculations since it is more rigorous.

Phonon spectrum of phosphorene generated from VASP is illustrated in Fig. 2. The different modes are numbered according to Ref. 31. Phonon modes 2 and 3 stand for the acoustic branches, whereas 7, 9, and 11 denote the optical branches. The corresponding deformation potential values and the frequencies of the optical phonon branches are represented in Table I. Among the two acoustic modes, 2 is considered for transport across the AC direction, whereas 3 is considered for the ZZ direction. This is due to the dominance of the respective modes along the AC or ZZ direction as demonstrated in the contour plot of electron-phonon coupling elements and other deductions in Ref. 31. Zero order optical phonon modes are considered in transport calculations. The effect of first order optical modes on the total scattering rates is insignificant[31] with respect to zero order modes and thus not considered in this study.[32]

The electronic band dispersion is modeled using a two-band $\mathbf{k}\cdot\mathbf{p}$ hamiltonian,[30]

$$H(\mathbf{k}) \equiv \begin{bmatrix} E_c + \eta_c k_x^2 + \nu_c k_y^2 & \gamma_1 k_x + \beta k_y^2 \\ \gamma_1 k_x + \beta k_y^2 & E_v + \eta_v k_x^2 + \nu_v k_y^2 \end{bmatrix}, \quad (1)$$

where $\mathbf{k} = (k_x, k_y)$ is the in-plane wave vector; $\eta_{c(v)}$, $\nu_{c(v)}$, and $\gamma_1$ are the fitting parameters, and $E_c$ and $E_v$ are the conduction band minimum and valence band maximum. The eigen values of the hamiltonian are calibrated against the DFT generated dispersion by choosing appropriate values of the fitting parameters, as shown in Table II. It is found (see Fig. 3) that band dispersion obtained from single band effective mass hamiltonian matches DFT data in a small energy window, whereas the band dispersion from two-band hamiltonian shows excellent match over a broad energy spectrum (0.5 eV) suitable for transport calculations in both MOSFETs and TFETs. We compare our methodology with that of Ref. 15 and present the results in Fig. 4. It is seen that the $I_D$-$V_G$ characteristics follow a similar trend with the ON-state current differing by an amount of 19.4%. Given that different DFT functionals (HSE in our work in contrast to GGA-PBE in Ref. 15) are used for crystal structure relaxation and subsequent band structure calculations, in conjunction with a 3D atomistic and full-band structure model (Ref. 15) in contrast to 2D low energy hamiltonian considered in our work, such difference can be acceptable. It should also be noted that our model captures the effect of intrinsic scattering in phosphorene FETs and excludes the effect of dielectric and interfacial environment.

For transport calculation, the NEGF equations are solved self-consistently with Poisson's equation. Assumption of translational invariance in the $y(x)$ direction of the device (according to the direction of transport, i.e., AC or ZZ) enables expressing the hamiltonian function and Green's function in terms of the in-plane transversal wave vector $k_{y(x)}$.

For each wave vector $k_{y(x)}$, the retarded Green's function (expressed in the matrix notation) is calculated at each energy $E$ as[33–35]

$$G^r(k_{y(x)}, E) = \left[(E-U)\mathrm{I} - H(k_{y(x)}) - \Sigma_S^r - \Sigma_D^r - \Sigma_{ph(ac)}^r - \Sigma_{ph(op)}^r\right]^{-1}, \quad (2)$$

where $U$ is the electrostatic potential in the device, I is the identity matrix, $H(k_{y(x)})$ is the hamiltonian matrix discretized along the transport direction $x(y)$, $\Sigma_S^r$ and $\Sigma_D^r$ are retarded self-energy matrices associated to the source/drain contacts,[33] and $\Sigma_{ph(ac)}^r$ and $\Sigma_{ph(op)}^r$ are the retarded self-energy matrices due to the interaction between carriers and acoustic (ac) and optical (op) phonons, respectively. From the retarded Green's function $G^r(k_{y(x)}, E)$ in Eq. (2), one can calculate the lesser ($<$) and greater ($>$) Green's

**TABLE I.** Values of deformation potentials $\Xi_{ac/op}$ (in unit $10^8$ eV/cm for optical and in eV for acoustic) and phonon energies $\hbar\omega_{ph}$ (in meV) for various branches of Fig. 2, both electrons and holes. Note that these values are taken from Ref. 31.

| | Acoustic | | | | Optical | | | | | |
|---|---|---|---|---|---|---|---|---|---|---|
| | 2 (AC) | | 3 (ZZ) | | 7 | | 9 | | 11 | |
| Parameter | Electron | Hole | Electron | Hole | Electron | Hole | Electron | Hole | Electron | Hole |
| $\Xi_{ac/op}$ | 2.74 | 4.21 | 8.31 | 1.83 | 8.07 | 1.22 | 6.60 | 3.81 | 6.60 | 3.81 |
| $\hbar\omega_{ph}$ | … | … | … | … | 42.1 | | 51.9 | | 55.0 | |

**TABLE II.** Values for $\mathbf{k}\cdot\mathbf{p}$ hamiltonian parameters used in transport calculations and effective mass for electrons (e) and holes (h).

| Calibrated parameters for $\mathbf{k}\cdot\mathbf{p}$ hamiltonian | | | | | | Effective mass | |
|---|---|---|---|---|---|---|---|
| $\eta_c$ (eVÅ$^2$) | $\eta_v$ (eVÅ$^2$) | $v_c$ (eVÅ$^2$) | $v_v$ (eVÅ$^2$) | $\gamma_1$ (eVÅ) | $\beta$ (eVÅ$^2$) | $m_x$ ($m_0$) | $m_y$ ($m_0$) |
| 1.34 | 2.61 | 2.91 | 0.63 | 5.82 | 3.72 | 0.17 (e), 0.16 (h) | 1.29 (e), 5.96 (h) |

functions, $G^{\lessgtr}(k_{y(x)}, E)$, as follows:

$$G^{\lessgtr}(k_{y(x)}, E) = G^{r}(k_{y(x)}, E)\left[\Sigma_{S}^{\lessgtr}(k_{y(x)}, E) + \Sigma_{D}^{\lessgtr}(k_{y(x)}, E) + \Sigma_{ph(ac)}^{\lessgtr}(k_{y(x)}, E) + \Sigma_{ph(op)}^{\lessgtr}(k_{y(x)}, E)\right] G^{r\dagger}(k_{y(x)}, E), \quad (3)$$

where $\Sigma_{S/D}^{\lessgtr}$ are the lesser ($<$) and greater ($>$) self-energies in the source (S) and drain (D) contacts, calculated as

$$\Sigma_{S/D}^{<} \equiv (\Sigma_{S/D}^{r} - \Sigma_{S/D}^{r\dagger}) \cdot f_{S/D},$$
$$\Sigma_{S/D}^{>} \equiv (\Sigma_{S/D}^{r} - \Sigma_{S/D}^{r\dagger}) \cdot (1 - f_{S/D}). \quad (4)$$

Here, † denotes the conjugate transpose and $f_{S/D}$ represents the Fermi-Dirac distribution function in the source/drain. $\Sigma_{ph(ac)}^{\lessgtr}$ and $\Sigma_{ph(op)}^{\lessgtr}$ in Eq. (3) stand for the acoustic and optical scattering self energies, respectively. The dissipative transport is treated within the self-consistent Born approximation (SCBA). Under such approximation, the lesser ($<$) and greater ($>$) self-energies for acoustic and optical phonon interaction are[34,35] given as follows. Only the diagonal elements of Green's function are considered based on the assumption that carrier-phonon interactions are local,

$$\Sigma_{ph(ac)}^{\lessgtr}(j, j, E) = \sum_{k_{y(x)}} \sum_{v} D_{v(ac)} G^{\lessgtr}(j, j, k_{y(x)}, E),$$
$$\Sigma_{ph(op)}^{\lessgtr}(j, j, E) = \sum_{k_{y(x)}} \sum_{v} D_{v(op)} \left(N_B + \frac{1}{2} \pm \frac{1}{2}\right) \quad (5)$$

$$G^{\lessgtr}(j, j, k_{y(x)}, E \pm \hbar\omega_{ph}), \quad (6)$$

where $j$ is the position index of the lattice grid point, $v$ is the phonon mode, $\omega_{ph}$ is the phonon frequency, $N_B = [\exp(\hbar\omega_{ph}/k_BT) - 1]^{-1}$ is the Bose factor for phonon occupancy, and $D_{v(ac/op)}$ denotes the square of the electron-phonon matrix element from the deformation potential theory. The terms $D_{v(ac/op)}$ in Eqs. (5) and (6) are determined as

$$D_{v(ac)} = \Xi_{ac}^2 k_B T/\rho V v_p^2,$$
$$D_{v(op)} = \Xi_{op}^2 \hbar^2/2\rho V E_{ph}, \quad (7)$$

where $\Xi_{ac}$ and $\Xi_{op}$ denote the acoustic and optical deformation potential constants (see Table I), ρ is the volumetric mass density of the material, V is the discretization mesh volume, $v_p$ is the sound velocity, and $E_{ph}$ denotes the optical phonon energy (equivalent to $\hbar\omega_{ph}$ in Table I). ρ is calculated as $1.39 \times 10^{-7}$ g/cm$^2$, and the values of deformation potentials and sound velocities are used as reported in Ref. 31. The retarded self-energies for both acoustic (ac)

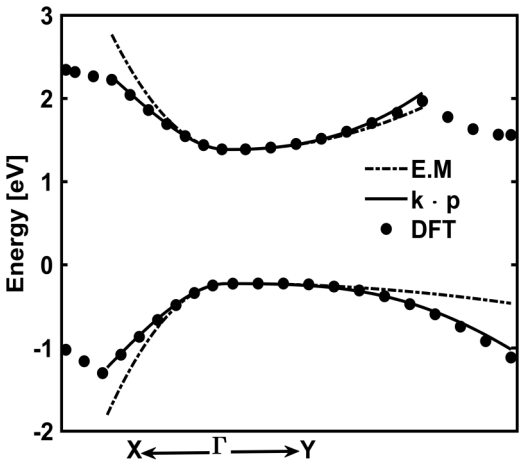


**FIG. 3.** Fitting of the band structure from model hamiltonian with DFT generated band dispersion. The eigenvalues from two-band hamiltonian show excellent match over an energy interval of 0.5 eV, whereas the single band effective mass (EM) hamiltonian deviates from the actual dispersion.

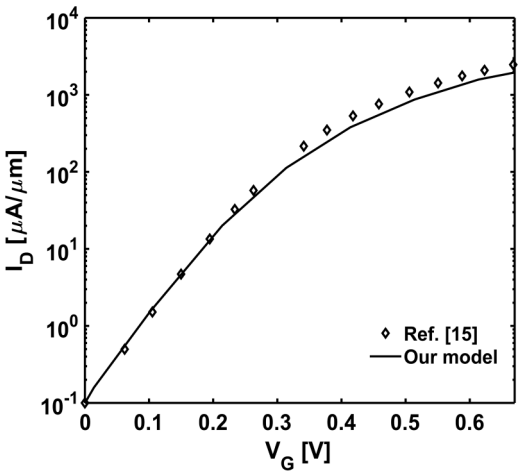


**FIG. 4.** Comparison of transfer characteristics using our transport model vs Ref. 15 for the same device configuration. Please note that the value of the dielectric constant of phosphorene is not reported in Ref. 15. Therefore, we consider the same value used in our work, i.e., 1.12.

and optical (op) phonon scattering are calculated as[35,36]

$$\Sigma^{r}_{ph(ac)}(j,j,E) = \sum_{k_{y(x)}}\sum_{\nu} D_{\nu(ac)} G^{r}(j,j,k_{y(x)},E), \tag{8}$$

$$\begin{aligned}\Sigma^{r}_{ph(op)}(j,j,E) = \sum_{k_{y(x)}}\sum_{\nu} D_{\nu(op)}\Big[&(N_B+1)G^{r}(j,j,k_{y(x)},E+\hbar\omega_{ph})\\ &+N_B G^{r}(j,j,k_{y(x)},E-\hbar\omega_{ph})\\ &+\frac{1}{2}\big(G^{<}(j,j,k_{y(x)},E-\hbar\omega_{ph})\\ &-G^{>}(j,j,k_{y(x)},E+\hbar\omega_{ph})\big)\Big].\end{aligned} \tag{9}$$

It should be noted that the real part of the retarded scattering self-energies has been neglected in our simulations, as it mainly contributes to an energy renormalization.[38–40] The interdependence between the scattering self-energies and Green's functions demands for an iterative solution of Eqs. (2)–(9) until self-consistency is reached by preserving the charge and current conservation laws.[37] In order to accelerate such self-consistent loop, the recursive Green's function algorithm is used.[34,41] Once the self-consistent Born approximation loop is converged, the electron and hole densities are determined from Green's functions $G^{\lessgtr}$ as

$$\begin{aligned} n(j,j) &\equiv \frac{1}{2\pi}\sum_{k_{y(x)}}\int_{-\infty}^{+\infty} G^{<}(j,j,k_{y(x)},E)dE,\\ p(j,j) &\equiv \frac{1}{2\pi}\sum_{k_{y(x)}}\int_{-\infty}^{+\infty} G^{>}(j,j,k_{y(x)},E)dE.\end{aligned} \tag{10}$$

The current density from position $j$ to $j+1$ along the $x(y)$ direction is calculated from the off-diagonal elements $(j, j+1)$ of $G^{\lessgtr}(i,j,k_{y(x)},E)$ as

$$\begin{aligned}J^{\lessgtr}(j,j+1) \equiv \sum_{k_{y(x)}}\frac{2q}{\hbar S}\int_{-\infty}^{+\infty}\frac{dE}{2\pi}[&H(j,j+1)G^{\lessgtr}((j+1,j),\\ &k_{y(x)},E) - H(j+1,j)G^{\lessgtr}((j,j+1),k_{y(x)},E)],\end{aligned} \tag{11}$$

where $H(j,j+1)$ corresponds to the nearest neighbor hopping terms in the discretized hamiltonian. The finite volume method is used to discretize the 2D Poisson's equation across the device cross section shown in Fig. 1. Dirichlet boundary conditions are enforced at the metal gate electrodes, whereas Neumann boundary conditions are used on rest of the edges to satisfy charge neutrality.

## III. RESULTS AND DISCUSSIONS

### A. Effect of individual phonon modes

We first discuss the effect of different phonon branches, both optical and acoustic, on the drain current of n- and p-MOSFETs. Figures 5(a)–5(d) show the dissipative and ballistic transfer characteristics of n- and p-type MOSFETs for AC and ZZ directions. In n-channel phosphorene MOSFETs, inelastic optical phonon scattering plays the most important role in the degradation of ON-state characteristics along both directions. Figures 5(a) and 5(b) depict that ON-state current is affected largely by the interaction between electron and optical phonon mode 7 in both n-AC and n-ZZ MOSFETs. The reason behind this phenomenon lies in the fact that optical phonon branch 7 has the highest deformation potential value and the lowest phonon energy (see Table I), which leads to increased backscattering of carriers through both emission and absorption[42] of phonons. On the other hand, remaining optical modes with higher phonon energy and smaller deformation potential can only backscatter through emission, resulting in reduced current loss.

However, in p-channel MOSFETs, the interaction between holes and optical phonon branches 9 and 11 strongly affects transport along both AC and ZZ as shown in Figs. 5(c) and 5(d). Indeed, phonon modes 9 and 11 have higher values of deformation potential than mode 7 in the valence band (see Table I) and thus higher contribution in the total scattering rate of holes.[31] Figures 5(c) and 5(d) also demonstrate some interesting phenomenon with respect to acoustic scattering in p-MOSFETs. From Fig. 5(d), it is found that the effect of scattering between holes and acoustic phonon branch 3 is minimal on the total drain current loss of p-ZZ MOSFET. However, the interaction between holes and acoustic phonon branch 2 results in severe degradation of drain current in p-AC MOSFET [see Fig. 5(c)]. This phenomenon is attributed to the value of acoustic phonon deformation potential along the AC (i.e., hole-phonon mode 2) direction, which is four times larger than the value along the ZZ (i.e., hole-phonon mode 3) direction (see Table I). It is further observed from Fig. 5(c) that contribution of acoustic phonon branch 2 becomes comparable to one of optical branches 9 and 11 in p-AC MOSFET. This entails from comparable values of deformation potential of acoustic mode 2 and optical modes 9 and 11 in the valence band of phosphorene.

Nonetheless, all the devices, n (AC and ZZ) and p (AC and ZZ) exhibit stronger effect of carrier-phonon scattering in the strong inversion region compared to the weak inversion region. At higher $V_G$, the top of the barrier in both n- and p-MOSFETs along both directions is pushed below the source Fermi level. This results in increased backscattering by optical phonons and significant loss of drain current $I_D$ in the strong inversion region with respect to the subthreshold regime.

Additional insights on dissipative transport of phosphorene MOSFETs are provided in Secs. III B and III C by comparing (i) the same direction but different channel dopings (i.e., n-AC, p-AC and n-ZZ, p-ZZ MOSFETs) and (ii) similar channel doping but different directions of transport (i.e., n-AC, n-ZZ and p-AC, p-ZZ MOSFETs).

### B. Scattering in MOSFETs with different channel types in a given transport direction

Phosphorene MOSFETs along a given direction with different channel types, i.e., n or p, depict significant difference in ON-current [compare Figs. 5(a) to 5(c), and 5(b) to 5(d).].

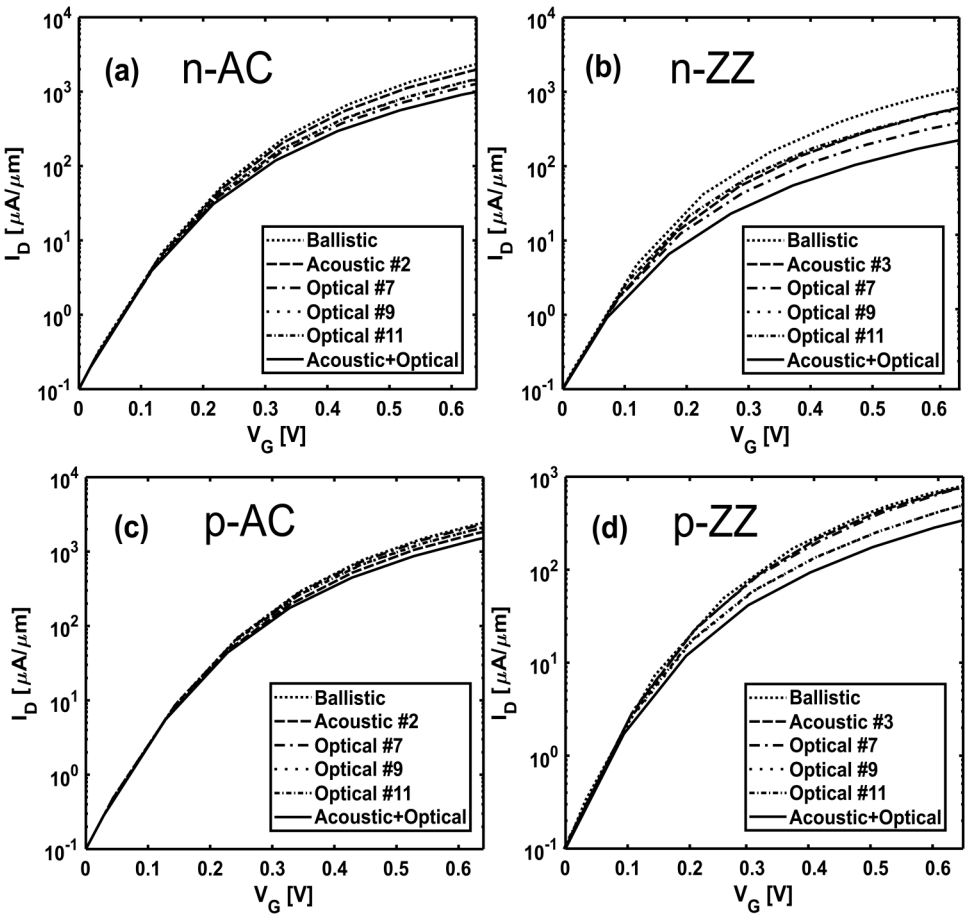


**FIG. 5.** Simulated transfer characteristics of phosphorene n-MOSFETs along (a) armchair (AC) and (b) zigzag (ZZ) directions and p-MOSFETs along (c) AC and (d) ZZ directions. In the ballistic regime, Poisson's equation does not converge anymore above $V_G$ = 0.5V along zigzag directions due to oscillations in the source region.[37] Ballistic current values are then obtained by extrapolation for $V_G$ above 0.5V.

This is reflected from the values of ballisticity of drain current, which is calculated as Ballisticity% = $[I_D(\text{dissipative})/I_D(\text{ballistic})]$. Magnitude of ON-current is almost similar for n- and p-MOSFETs along the AC direction (2.34 mA/$\mu$m and 2.46 mA/$\mu$m, respectively) in the ballistic regime due to comparable values of effective mass. However, the ballisticity for n-AC MOSFET in the scattering regime is 42%, whereas for p-AC MOSFET, it is 63%, which implies greater change of $I_D$(dissipative) from $I_D$(ballistic) in n-AC than p-AC MOSFETs. This difference in dissipative ON-state current arises due to higher values of deformation potential for optical phonon modes in the conduction band than in the valence band (see Table I). The effective mass of holes is approximately 4.5 times larger than electrons along the zigzag direction. As a consequence, ballistic ON-current in p-ZZ MOSFET is significantly less than n-ZZ MOSFET (0.8 mA/$\mu$m and 1.12 mA/$\mu$m, respectively). However, p-ZZ MOSFET surpasses n-ZZ MOSFET in terms of ballisticity by a significant amount (42.5% in p-ZZ and 20% in n-ZZ). This results from sufficiently lower values of deformation potential along the ZZ direction, of both acoustic and optical phonon modes in the valence band than in the conduction band (see Table I). Overall, it could be concluded that n-type phosphorene MOSFETs undergo stronger scattering with respect to their p-channel counterparts and hence demonstrate poor ballisticity. It should be noted that all ballisticity calculations are performed using ballistic converged potential, which is reported to include artificial lowering of the conduction band at high gate bias.[37] As a result, we recalculated the ballisticities using the potential containing phonon scattering.[37] The values of the ballistic currents are lowered (1.7 mA/$\mu$m, 2.1 mA/$\mu$m, 0.9 mA/$\mu$m, and 0.45 mA/$\mu$m for n-AC, p-AC, n-ZZ, and p-ZZ MOSFETs, respectively). The new ballisticity values of n-AC, p-AC, n-ZZ, and p-ZZ MOSFETs are 56%, 70%, 25%, and 53%, respectively. However, the overall conclusion regarding better performant devices in terms of ballisticity remains unchanged.

### C. Scattering in MOSFETs with different transport directions for a given channel type

Next, we compare the transfer characteristics in phosphorene MOSFETs with a given channel doping (n or p) but different directions of transport [compare Figs. 5(a) to 5(b), and 5(c) to 5(d).]. These figures suggest that scattering starts to dominate the transfer characteristics in both n- and p-ZZ MOSFETs from lower values of gate voltage, $V_G$, in contrast to their AC counterparts. In other words, the effect of scattering is stronger in the case of phosphorene MOSFETs along the zigzag direction of transport. This phenomenon is explained with the help of Fig. 6, which shows

conduction band profiles for both AC and ZZ n-type devices. It should be noted that, though Fig. 6 shows only n-MOSFETs, similar argument applies for p-MOSFETS. Along the ZZ direction, the transport effective mass is higher, whereas the transverse effective mass is lower. Higher transport effective mass entails poor transmission and lower transverse effective mass leads to smaller density of states. Both of these effects result in lower values of drain current $I_D$. Therefore, ZZ MOSFETs require a smaller potential barrier in order to ensure the same $I_D$ of AC MOSFETs. As a consequence, the difference between the source fermi level $E_{fS}$ and top of the barrier, $\eta_{fS}$, is greater along the ZZ direction [see Fig. 6(a)], and the effect of optical phonon backscattering becomes more important[43] in phosphorene ZZ MOSFETs. Current spectrum plots in Figs. 6(b) and 6(c) also show that the inelastic emission process is stronger for ZZ MOSFET. This induces a decrease of the effective carrier velocity [calculated as $v_{drift} = I_D/(q \times \text{Charge})$, where q is the electronic charge] with respect to the AC device [see Fig. 6(d)] and subsequent space charge accumulation at the source end. It leads to significant modulation of the channel potential and intensifies the scattering and current loss mechanism.[42] Therefore, ZZ MOSFETs demonstrate poor performance under the dissipative regime irrespective of the type of channel doping, i.e., n or p.

We also compare our results with a similar study reported for $MoS_2$ n-MOSFETs.[44] $MoS_2$ unlike phosphorene exhibits directionally invariant effective mass and phonon deformation potential.[44] Comparison of deformation potential values of $MoS_2$ reported in Ref. 44 with those of phosphorene suggests higher values of optical deformation potential constants in the case of phosphorene. Thus, degradation of ON-current in $MoS_2$ n-MOSFET is lower with respect to phosphorene-AC n-MOSFET. This is indeed reflected in the ballisticity of $MoS_2$ n-MOSFET (65%[44]) compared to phosphorene-AC n-MOSFET (42%).

Aggressive scaling of channel lengths in MOSFET results in an increase of OFF-current in MOSFET as the subthreshold swing is limited by the thermionic emission to 60 mV/dec. TFET is a gated p-i-n diode, which relies on the mechanism of band to band tunneling (BTBT) for the injection of carriers. This ensures the bandpass filtering of high energy tails of the source Fermi function, which might result in low OFF-current and sub-60 mV/dec subthreshold slope. The complex band structure of a material could provide useful guideline for its suitability as high-performance TFET channel material. Wrapping of imaginary bands between conduction and valence band edges implies higher BTBT probability.[45] Estimate of BTBT probability under Wentzel–Kramers–Brillouin approximation could be obtained from the area covered under the wrapped imaginary band (known as the least action integral), which is usually small in the case of low effective mass materials.[45]

### D. Complex band structure

The complex band structure of phosphorene along [100], i.e., the AC direction in Fig. 7(a) shows complete wrapping between the conduction band and valence band edges, implying weak phonon-assisted tunneling (PAT). On the contrary, there are

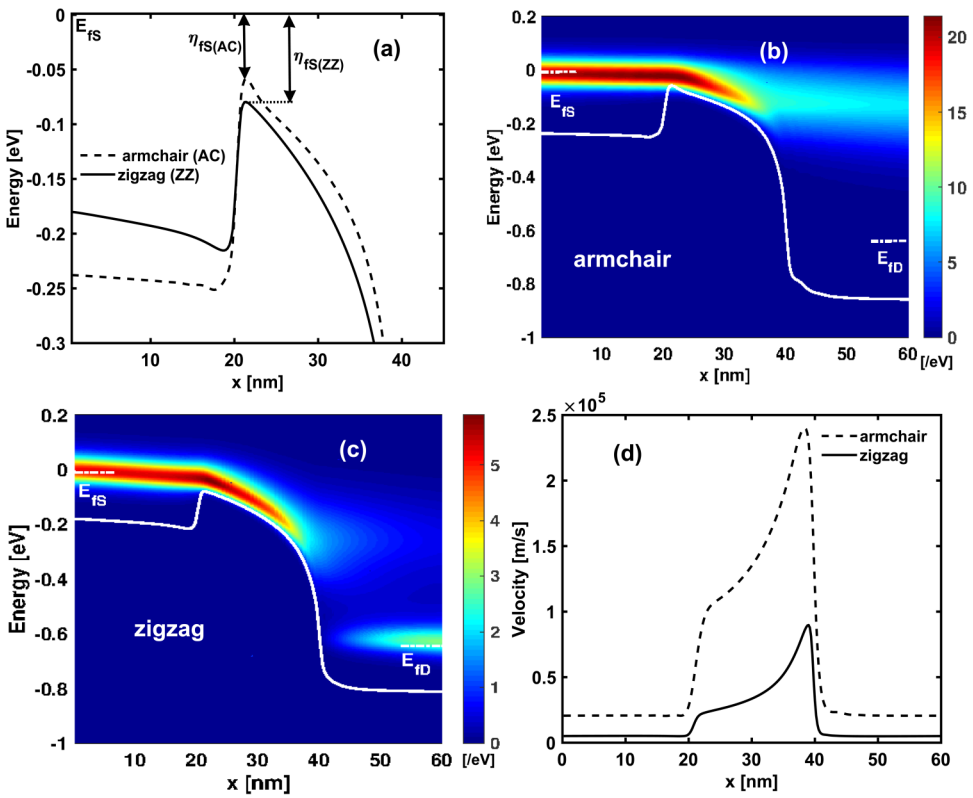


**FIG. 6.** (a) Potential barrier profile of n-MOSFET along AC and ZZ directions. It should be noted that the source potential profile bending at the ON-state arises due to the filling of states below the source contact by phonon emission, which ultimately leads to better convergence.[37] $\eta_{fS(ZZ(AC))}$ denotes the distance between the source Fermi level and top of the barrier along ZZ (AC). Since $\eta_{fS(ZZ)} > \eta_{fS(AC)}$, it results in increased backscattering and drain current loss along the zigzag transport direction. Energy resolved current spectrum superimposed on the conduction band edge profile along (b) AC and (c) ZZ directions. (d) Carrier drift velocity across the device length along both directions.

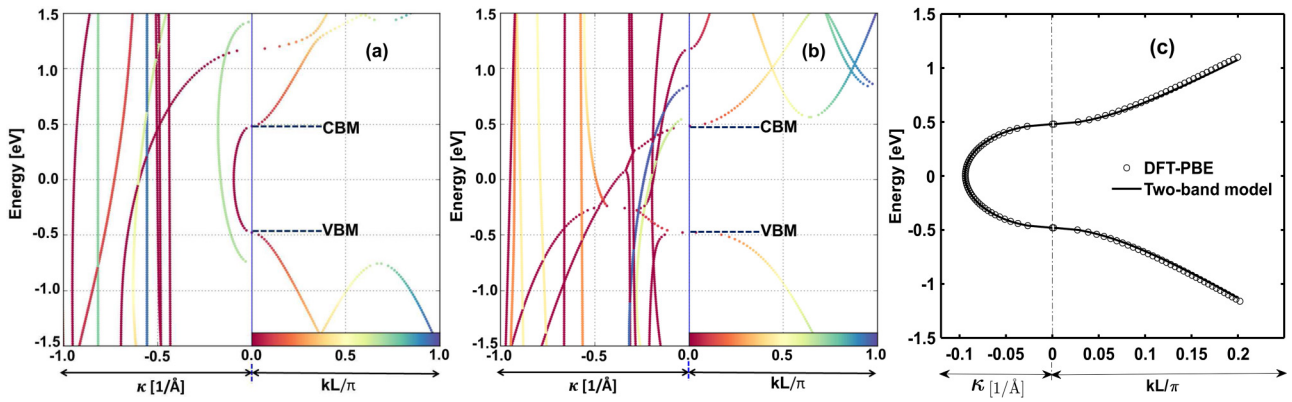


**FIG. 7.** Complex band structure along (a) [100], i.e., armchair and (b) [010], i.e., zigzag directions. The right-hand panel illustrates the real bands, where the solution **k** is normalized by the perpendicular layer separation L. The left hand panel portrays the complex bands against reciprocal Cartesian coordinates on the x axis. There is complete wrapping of imaginary bands between the conduction band minimum (CBM) and the valence band maximum (VBM) along the armchair direction. However, the imaginary bands along the zigzag direction show multiple crossings between CBM and VBM. (c) Comparison of the imaginary band dispersion obtained from ATK LCAO-PBE simulations against the recalibrated two-band **k** · **p** model along the armchair direction.

multiple crossings of imaginary bands between the conduction band minimum and valence band maximum in ZZ phosphorene as shown in Fig. 7(b). Some imaginary bands are close together with the energy difference less than the energy of optical phonon $\hbar\omega_{ph}$. This translates to strong phonon-assisted tunneling (PAT) along the ZZ direction at OFF-state.[46] Treatment of multiple imaginary band crossings on TFET transfer characteristics is outside the scope of this paper since it should be calculated by considering a

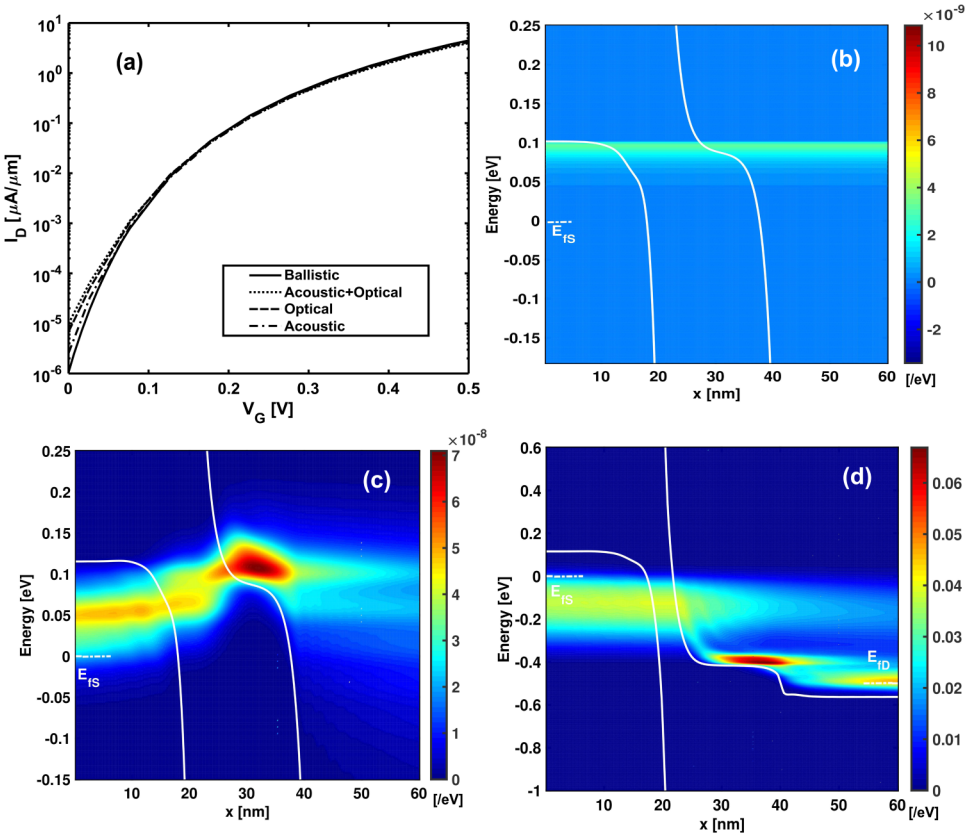


**FIG. 8.** (a) $I_D$-$V_G$ plot for p-i-n TFET. (b) Energy resolved current spectrum superimposed on the conduction band edge profile for phosphorene TFET along the AC direction in the ballistic regime at OFF-state. (c) Same as (b) in the dissipative regime at OFF-state and (d) same as (c) in the dissipative regime at ON-state. OFF-state current in ballistic TFET yields lower values due to the presence of higher tunneling barrier. However, in the dissipative regime, OFF-current rises under the action of phonon absorption at the source-channel interface. On the other hand, in the ON-state, negligible amount of carriers can backscatter into the drain due to high potential barrier at the junction of the channel and drain.

hamiltonian spanning more than two bands. For completeness, a comparison between the imaginary band dispersion using the two-band model and the ATK calculations is shown in Fig. 7(c) along the armchair direction. It should be noted that complex bands are generated from ATK using PBE functional, whereas the real bands (shown in Fig. 3) are calibrated against HSE functional based DFT calculations. As a result, the fitting parameters of the hamiltonian are recalibrated against the LCAO-PBE band structure. The values of the fitting parameters are $\eta_c = 1.70$ eV Å$^2$, $\eta_v = 3.53$ eV Å$^2$, $\nu_c = 1.01$ eV Å$^2$, $\nu_v = 0.11$ eV Å$^2$, $\gamma_1 = 5.05$ eV Å, and $\beta = 1.68$ eV Å$^2$. The obtained complex band structure shows wrapping of the imaginary bands and is in good agreement with the LCAO-PBE imaginary bands, thereby validating the considered two-band model again.

### E. Phonon scattering in n-AC tunnel FET

However, the transport calculation based on a two-band $\mathbf{k}\cdot\mathbf{p}$ hamiltonian is sufficient for the cases where the imaginary band wraps itself between conduction and valence band edges.[47] The transfer characteristics of phosphorene TFET along the AC direction as obtained from self-consistent transport calculations shows nominal effect of PAT throughout the gate bias window [see Fig. 8(a)] and dominance of optical phonon modes with respect to acoustic modes.

Figure 8(a) also shows that OFF-current changes by one decade under PAT, with respect to ballistic transport. However, the change in the subthreshold swing spans over a very small region of gate voltage (approximately 0.1 V), and the dissipative $I_D$ quickly catches up with the ballistic $I_D$. The result is in agreement with our conclusion made from the CBS of AC phosphorene. The increase in OFF-current is explained next with the help of potential profile bending at the source-channel interface. At low gate bias, band bending at the source-channel interface is not severe enough to facilitate direct tunneling in contrast to the ballistic case [see Fig. 8(b)]. However, OFF-current rises because transmission of carriers mostly occurs by phonon absorption at the source side, which thermalizes on reaching the drain contact[46,48] as depicted in Fig. 8(c). On the other hand, at high gate bias, the effect of PAT diminishes. The conduction band in the channel is pushed well below the valence band in the source, and transmission is dominated by direct BTBT as shown in Fig. 8(d). The optical phonons that are emitted at the drain region are not able to backscatter into the source due to the presence of a large potential barrier at the channel-drain junction. As a result, there is negligible current loss at ON-state, which is just opposite of MOSFET.

## IV. CONCLUSION

The effect of different types of electron-phonon coupling on the transfer characteristics of phosphorene n- and p-MOSFETs along both AC and ZZ directions is investigated through self-consistent NEGF-SCBA equations. Results suggest that the zero order optical phonon mode having the highest deformation potential constant and the lowest energy bears the strongest effect on degradation of ON-current by scattering in all the devices except p-AC MOSFET. The effect of carrier-phonon scattering is found to be more pronounced in transport along the ZZ direction than the AC direction for MOSFETs of similar channel doping. However, in the dissipative regime and in terms of ballisticity along a fixed direction of carrier transport, p-MOSFETs outperform n-MOSFETs and thus are more suitable candidates for realistic phosphorene-based, high-performance FETs. The complex band structure of phosphorene showing unique characteristics along each of the two directions (AC and ZZ) is reported. It suggests that BTBT probability along the ZZ direction would be hugely compromised due to multiple imaginary band crossings inside the bandgap. However, the effect of scattering on PAT is found to be minimal for AC TFET in terms of subthreshold swing.

## ACKNOWLEDGMENTS

This work was supported in part by the Science and Engineering Research Board, Department of Science and Technology, Government of India under Grant No. SB/S3/EECE/0209/2015 and in part by the Council for Scientific and Industrial Research under Grant No. 22(0765)/18/EMR-II.

## REFERENCES

[1]B. Radisavljevic, M. B. Whitwick, and A. Kis, "Integrated circuits and logic operations based on single-layer $MoS_2$," ACS Nano **5**, 9934–9938 (2011).
[2]S. B. Desai, S. R. Madhvapathy, A. B. Sachid, J. P. Llinas, Q. Wang, G. H. Ahn, G. Pitner, M. J. Kim, J. Bokor, C. Hu *et al.*, "$MoS_2$ transistors with 1-nanometer gate lengths," Science **354**, 99–102 (2016).
[3]H. Fang, S. Chuang, T. C. Chang, K. Takei, T. Takahashi, and A. Javey, "High-performance single layered $WSe_2$ p-FETs with chemically doped contacts," Nano Lett. **12**, 3788–3792 (2012).
[4]L. Li, Y. Yu, G. J. Ye, Q. Ge, X. Ou, H. Wu, D. Feng, X. H. Chen, and Y. Zhang, "Black phosphorus field-effect transistors," Nat. Nanotechnol. **9**, 372 (2014).
[5]H. Liu, A. T. Neal, Z. Zhu, Z. Luo, X. Xu, D. Tománek, and P. D. Ye, "Phosphorene: An unexplored 2D semiconductor with a high hole mobility," ACS Nano **8**, 4033–4041 (2014).
[6]K. Novoselov, D. Jiang, F. Schedin, T. Booth, V. Khotkevich, S. Morozov, and A. Geim, "Two-dimensional atomic crystals," Proc. Natl. Acad. Sci. U.S.A. **102**, 10451–10453 (2005).
[7]W. Lu, H. Nan, J. Hong, Y. Chen, C. Zhu, Z. Liang, X. Ma, Z. Ni, C. Jin, and Z. Zhang, "Plasma-assisted fabrication of monolayer phosphorene and its Raman characterization," Nano Res. **7**, 853–859 (2014).
[8]Z. Guo, H. Zhang, S. Lu, Z. Wang, S. Tang, J. Shao, Z. Sun, H. Xie, H. Wang, X.-F. Yu *et al.*, From black phosphorus to phosphorene: Basic solvent exfoliation, evolution of Raman scattering, and applications to ultrafast photonics," Adv. Funct. Mater. **25**, 6996–7002 (2015).
[9]L. Kou, C. Chen, and S. C. Smith, "Phosphorene: Fabrication, properties, and applications," J. Phys. Chem. Lett. **6**, 2794–2805 (2015).
[10]X. Luo, Y. Rahbarihagh, J. C. Hwang, H. Liu, Y. Du, and D. Y. Peide, "Temporal and thermal stability of $Al_2O_3$-passivated phosphorene MOSFETs," IEEE Electron Device Lett. **35**, 1314–1316 (2014).
[11]N. Haratipour, S. Namgung, S.-H. Oh, and S. J. Koester, "Fundamental limits on the subthreshold slope in Schottky source/drain black phosphorus field-effect transistors," ACS Nano **10**, 3791–3800 (2016).
[12]X. Cao and J. Guo, "Simulation of phosphorene field-effect transistor at the scaling limit," IEEE Trans. Electron Devices **62**, 659–665 (2015).
[13]H. Ilatikhameneh, T. Ameen, B. Novakovic, Y. Tan, G. Klimeck, and R. Rahman, "Saving Moore's law down to 1 nm channels with anisotropic effective mass," Sci. Rep. **6**, 31501 (2016).
[14]R. Quhe, Q. Li, Q. Zhang, Y. Wang, H. Zhang, J. Li, X. Zhang, D. Chen, K. Liu, Y. Ye *et al.*, "Simulations of quantum transport in sub-5-nm monolayer phosphorene transistors," Phys. Rev. Appl. **10**, 024022 (2018).

[15]A. Szabo, R. Rhyner, H. Carrillo-Nunez, and M. Luisier, "Phonon-limited performance of single-layer, single-gate black phosphorus n-and p-type field-effect transistors," in *2015 IEEE International Electron Devices Meeting (IEDM)* (IEEE, 2015), pp. 12.1.1–12.1.4.
[16]M. Luisier, A. Szabo, C. Stieger, C. Klinkert, S. Brück, A. Jain, and L. Novotny, "First-principles simulations of 2-D semiconductor devices: Mobility, IV characteristics, and contact resistance," in *2016 IEEE International Electron Devices Meeting (IEDM)* (IEEE, 2016), pp. 5.4.1–5.4.4.
[17]M. Brahma, A. Kabiraj, and S. Mahapatra, "Insights on anisotropic dissipative quantum transport in n-type phosphorene MOSFET," in *2019 32nd International Conference on VLSI Design and 2019 18th International Conference on Embedded Systems (VLSID 2019)* (IEEE, 2019), pp. 179–184.
[18]See http://www.itrs2.net/2013-itrs.html for "International Technology Roadmap for Semiconductors" (last accessed November 26, 2018).
[19]V. Wang, Y. Kawazoe, and W. Geng, "Native point defects in few-layer phosphorene," Phys. Rev. B **91**, 045433 (2015).
[20]G. Kresse and J. Furthmüller, "Efficient iterative schemes for *ab initio* total-energy calculations using a plane-wave basis set," Phys. Rev. B **54**, 11169 (1996).
[21]G. Kresse and J. Furthmüller, "Efficiency of ab-initio total energy calculations for metals and semiconductors using a plane-wave basis set," Comput. Mater. Sci. **6**, 15–50 (1996).
[22]G. Kresse and D. Joubert, "From ultrasoft pseudopotentials to the projector augmented-wave method," Phys. Rev. B **59**, 1758 (1999).
[23]J. P. Perdew, K. Burke, and M. Ernzerhof, "Generalized gradient approximation made simple," Phys. Rev. Lett. **77**, 3865 (1996).
[24]J. Heyd, G. E. Scuseria, and M. Ernzerhof, "Hybrid functionals based on a screened Coulomb potential," J. Chem. Phys. **118**, 8207–8215 (2003).
[25]A. Togo and I. Tanaka, "First principles phonon calculations in materials science," Scr. Mater. **108**, 1–5 (2015).
[26]See http://quantumwise.com/ for "QuantumWise Atomistix ToolKit (ATK) with Virtual NanoLab" (last accessed November 26, 2018).
[27]D. Hamann, "Optimized norm-conserving Vanderbilt pseudopotentials," Phys. Rev. B **88**, 085117 (2013).
[28]M. Schlipf and F. Gygi, "Optimization algorithm for the generation of ONCV pseudopotentials," Comput. Phys. Commun. **196**, 36–44 (2015).
[29]J. Qiao, X. Kong, Z.-X. Hu, F. Yang, and W. Ji, "High-mobility transport anisotropy and linear dichroism in few-layer black phosphorus," Nat. Commun. **5**, 4475 (2014).
[30]A. Rodin, A. Carvalho, and A. C. Neto, "Strain-induced gap modification in black phosphorus," Phys. Rev. Lett. **112**, 176801 (2014).
[31]M. Elahi and M. Pourfath, "Ab initio effective deformation potentials of phosphorene and consistency checks," J. Phys. Condens. Matter **30**, 225701 (2018).
[32]K. Kaasbjerg, K. S. Thygesen, and K. W. Jacobsen, "Phonon-limited mobility in n-type single-layer $MoS_2$ from first principles," Phys. Rev. B **85**, 115317 (2012).
[33]S. Datta, *Quantum Transport: Atom to Transistor* (Cambridge University Press, 2005).
[34]M. Anantram, M. S. Lundstrom, and D. E. Nikonov, "Modeling of nanoscale devices," Proc. IEEE **96**, 1511–1550 (2008).
[35]M. Bescond, D. Logoteta, F. Michelini, N. Cavassilas, T. Yan, A. Yangui, M. Lannoo, and K. Hirakawa, "Thermionic cooling devices based on resonant-tunneling AlGaAs/GaAs heterostructure," J. Phys. Condens. Matter **30**, 064005 (2018).
[36]U. Aeberhard and R. Morf, "Microscopic nonequilibrium theory of quantum well solar cells," Phys. Rev. B **77**, 125343 (2008).
[37]M. Luisier and G. Klimeck, "Atomistic full-band simulations of silicon nanowire transistors: Effects of electron-phonon scattering," Phys. Rev. B **80**, 155430 (2009).
[38]A. Svizhenko and M. Anantram, "Role of scattering in nanotransistors," IEEE Trans. Electron Devices **50**, 1459–1466 (2003).
[39]S. Jin, Y. J. Park, and H. S. Min, "A three-dimensional simulation of quantum transport in silicon nanowire transistor in the presence of electron-phonon interactions," J. Appl. Phys. **99**, 123719 (2006).
[40]Y. Lee, M. Bescond, D. Logoteta, N. Cavassilas, M. Lannoo, and M. Luisier, "Anharmonic phonon-phonon scattering modeling of three-dimensional atomistic transport: An efficient quantum treatment," Phys. Rev. B **97**, 205447 (2018).
[41]R. Lake, G. Klimeck, R. C. Bowen, and D. Jovanovic, "Single and multiband modeling of quantum electron transport through layered semiconductor devices," J. Appl. Phys. **81**, 7845–7869 (1997).
[42]H. Tsuchiya and S.-i. Takagi, "Influence of elastic and inelastic phonon scattering on the drive current of quasi-ballistic MOSFETs," IEEE Trans. Electron Devices **55**, 2397–2402 (2008).
[43]S. O. Koswatta, S. Hasan, M. S. Lundstrom, M. Anantram, and D. E. Nikonov, "Non-equilibrium Green's function treatment of phonon scattering in carbon nanotube transistors," IEEE Trans. Electron Devices **54**, 2339–2351 (2007).
[44]L. Liu, Y. Lu, and J. Guo, "On monolayer $MoS_2$ field-effect transistors at the scaling limit," IEEE Trans. Electron Devices **60**, 4133–4139 (2013).
[45]R. K. Ghosh and S. Mahapatra, "Monolayer transition metal dichalcogenide channel-based tunnel transistor," IEEE J. Electron Devices Soc. **1**, 175–180 (2013).
[46]M. Luisier and G. Klimeck, "Simulation of nanowire tunneling transistors: From the Wentzel–Kramers–Brillouin approximation to full-band phonon-assisted tunneling," J. Appl. Phys. **107**, 084507 (2010).
[47]M. Brahma, A. Kabiraj, D. Saha, and S. Mahapatra, "Scalability assessment of Group-IV mono-chalcogenide based tunnel FET," Sci. Rep. **8**, 5993 (2018).
[48]S. O. Koswatta, M. S. Lundstrom, and D. E. Nikonov, "Influence of phonon scattering on the performance of p-i-n band-to-band tunneling transistors," Appl. Phys. Lett. **92**, 043125 (2008).